Results in Chemistry 29 (2026) 103752

Contents lists available at ScienceDirect

Results in Chemistry

journal homepage: www.sciencedirect.com/journal/results-in-chemistry

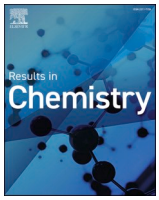

Effect of copper doping on $NiCo_2O_4$ nanostructures as anode material for enhanced electrochemical performance of lithium-ion batteries

Durga S. Nair [a,b], Reshma S. Babu [c], Bharath Chandran [c], Prasad Gonugunta [d], Thamayanthi Panneerselvam [c,e], Ramaswamy Murugan [c], Harish Kumar [b], Ruud Hendrikx [d], Arjan Cornet [d], Arjan Mol [d], N. Satyanarayana [c,*], Prasaanth Ravi Anusuyadevi [d,*]

[a] Department of Physics, Sree Narayana College, Chengannur, Alappuzha, India
[b] Department of Physics, Puducherry Technological University, Puducherry 605014, India
[c] Department of Physics, Pondicherry University, Puducherry 605014, India
[d] Department of Materials Science and Engineering (MSE), Faculty of Mechanical Engineering (ME), Delft University of Technology, Mekelweg 2, Delft 2628, CD, Netherlands
[e] Departments of Applied Physics and Science Education, Eindhoven University of Technology, Het Eeuwsel 53, 5612, AZ, Eindhoven, Netherlands

ARTICLE INFO

Keywords:
$NiCo_2O_4$
Cu doping
Microwave
Hydrothermal synthesis
Li-ion batteries

ABSTRACT

The surging demand for high-energy density lithium-ion batteries (LIBs) necessitates the exploration of anode materials with higher storage capacity. Nickel-cobalt (Ni—Co) based transition metal oxides (TMOs) are strong contenders due to their high theoretical capacity based on conversion reactions. The copper (Cu) doping strategy is adopted to improve the electrochemical performance through addressing the drawbacks of $NiCo_2O_4$, such as lower conductivity and volume expansion. In this work, Cu-doped $NiCo_2O_4$ nanomaterials are synthesized via a rapid, efficient, and scalable microwave-assisted synthesis route. When evaluated as an anode material for LIBs, the Cu-doped $NiCo_2O_4$ electrode delivers a high reversible specific capacity of 662 mAh g^{-1} at a current density of 100 mAg^{-1}. The enhanced performance is attributed to the unique porous nanorod-like structure with a high surface area of 59.4 m^2/g, which provides short lithium-ion diffusion pathways. Significantly, the copper acts as an inactive material that accommodates volume changes effectively during cycling when compared to pure $NiCo_2O_4$. Furthermore, the electrode exhibits an excellent rate capability and remarkable cycling stability. These findings indicate that copper doping is found to be an efficient approach for enhancing the cyclic performance of TMO-based anodes for next-generation LIBs.

1. Introduction

The development of alternative energy sources is critical to meet the urgent demands of our contemporary civilization and reduce our reliance on fossil fuels. LIBs unrivalled combination of high energy and power density makes them an ideal contender for portable electronics: cell phones, laptops, computers, etc., as well as for large-sized devices: electric vehicles (EV) and plug-in hybrid electric cars (PHEV) [1]. Intrinsically, LIBs have fundamental advantages over other battery chemistries [2]. Lithium has the lowest reduction potential (−3.04 V vs Standard Hydrogen Electrode (SHE)), giving LIBs the highest possible cell potential. Additionally, lithium is the third lightest element and has one of the smallest ionic radii among single-charged ions, resulting in high gravimetric, volumetric capacity, and power density for Lithium (Li)-based batteries. On the other hand, LIBs are currently relatively expensive for high-energy applications such as transportation and grid storage. Concurrently, the potential shortages of lithium and some transition metals could pose issues in the future.

Extensive research on the components and their component chemistries is performed widely for the betterment of the LIBs for high-energy storage applications. The studies on the cathode part have been ongoing for decades, and various high-performing cathode materials like $LiCoO_2$, $LiFePO_4$, $LiMn_2O_4$, $LiNiMnCoO_2$, etc., have been successfully employed in the market [3]. Since 1991, the first commercial LIBs have employed graphite as the anode material. Like for the cathode, anode materials with superior properties such as high specific capacity, long cycle life, smaller volume changes, low cost, and abundance are vital in LIBs, as it directly impacts the battery's electrochemical performance [4]. To

* Corresponding authors.
E-mail addresses: nallanis2011@gmail.com (N. Satyanarayana), P.RaviAnusuyadevi@tudelft.nl (P.R. Anusuyadevi).

https://doi.org/10.1016/j.rechem.2026.103752
Received 12 January 2026; Accepted 11 August 2026
Available online 12 August 2026

achieve the high energy density required for the current modern devices, anode materials should have a high lithium storage capacity, a low standard redox potential, and excellent electron and lithium-ion conductivity [5]. In anodes, lithium is stored through various mechanisms, including (i) intercalation/deintercalation, (ii) alloying/de-alloying, and (iii) conversion processes [4,6].

Among the three reaction mechanisms for lithium storage, the Li intercalation-deintercalation process displayed by materials such as graphite (372 mAh g^{-1}) and $Li_4Ti_5O_{12}$ (175 mAh g^{-1}) shows a limited capacity and raises concerns for battery safety operation, due to lithium dendrite formation [7,8]. Silicon anodes exhibiting a Li alloying-dealloying mechanism are exceptionally promising, with a specific capacity of 4200 mAh g^{-1}. However, large volume variation during continuous cycling limits the Si anode implementation for commercial use [9]. Conversion reaction materials, such as TMOs, have attracted much interest due to their multiple valences, high theoretical capacity, high power density, high corrosion resistance, low cost, and abundance. These materials have low lithium intercalation potential when compared to graphite anodes, which enhances the safety features, like thermal runaway, internal short circuit of the cell, etc., by inhibiting lithium dendrite formation [10].

TMOs displaying lithium storage through conversion reactions exhibit higher specific capacity than graphite [700–1050 mAh g^{-1}] [11,12]. Among mono transition metal oxides, Co_3O_4 shows a relatively high theoretical specific capacity of 890 mAh g^{-1} [13]. However, these mono-metal oxide materials face practical challenges, such as lower conductivity and significant volume fluctuations during cycling, causing a rapid decline in capacity during battery lifetime [14]. As a result, the study of binary transition metal oxides, isostructural to Co_3O_4, has become a promising anode material for LIBs. They effectively address the drawbacks of simple mono-oxides by combining two types of functional materials, creating a synergistic effect that enhances the intrinsic properties by facilitating rich redox chemistries and higher mechanical stability. Among them, the cobaltates such as $ZnCo_2O_4$ [15,16], $MnCo_2O_4$ [17,18], $CuCo_2O_4$ [19,20], $NiCo_2O_4$ [21,22], etc., are found to be potential candidates as anode material for lithium storage.

The inverse spinel $NiCo_2O_4$ shows a theoretical capacity of 890 mAh g^{-1}, has been demonstrated to have low diffusion resistance, higher structural stability, and easy electrolyte penetration [23]. It also exhibits high conductivity due to the presence of mixed valences [Ni^{2+}/Ni^{3+}, Co^{2+}/Co^{3+}] of the same cation [24]. The literature shows that the addition of Ni to the Co spinel structure ($Ni_xCo_{(3-x)}O_4$) shows an electrical conductivity of 0.1–0.3 S cm^{-1}, which is higher than Co_3O_4, which has an electrical conductivity of 3.1 × 10^{-5} S cm^{-1} [25]. Also, it can induce vacancies, providing active sites for the redox process, which can enhance lithium storage activities. However, $NiCo_2O_4$ exhibits inferior cyclability and irreversible capacity fading due to significant volume expansion and innate semiconductive nature [26]. The addition of impurity atoms in the sites of $NiCo_2O_4$ is considered to be an effective method to overcome these challenges [27,28]. Doping of cationic atoms, such as Mn, Zn, Al, Cu, etc., may provide numerous active sites and can tune the charge state and band gap of TMOs to enhance the conductivity and, thus, improve the electrochemical performances [29,30]. From the literature, it was found that copper doping induces a higher (energy level) electron state near the Fermi level of $NiCo_2O_4$ [31]. From our previous study, we observed that the addition of Cu to $NiCo_2O_4$ sites results in a decrease in bandgap, exhibiting an enhanced conductivity of $NiCo_2O_4$ and thereby improving the electrochemical performance as an electrocatalyst for Hydrogen Evolution Reaction (HER) [32].

In this context, this work focuses on improving the conductivity of $NiCo_2O_4$ electrodes for battery applications with copper dopants. Cu-doped $NiCo_2O_4$ materials were synthesized using a simple and cost-effective microwave-assisted hydrothermal method. From our previous studies on electrocatalysis, the optimized Cu doping concentration of 10% was chosen as it offers the most favorable physicochemical characteristics [32]. Here, we are utilizing the Cu doped $NiCo_2O_4$ as an anode material for lithium-ion batteries by fabricating a CR-2032-type half-cell, and we have successfully studied the effect of Cu doping on the cyclic performance of $NiCo_2O_4$.

2. Materials and methods

2.1. Synthesis of cu doped $NiCo_2O_4$ nanostructures

Cobalt chloride hexahydrate ($CoCl_2{\cdot}6H_2O$, 98%) was purchased from Sigma Aldrich. Nickel chloride hexahydrate ($NiCl_2{\cdot}6H_2O$, 99%), copper acetate monohydrate ($Cu(CH_3)COO_2.H_2O$), and Urea (99%) were purchased from SRL chemicals. All chemicals were used as received, without any further treatment. Double-distilled water was used for all synthesis steps in this study. Ternary Cu-doped $NiCo_2O_4$ inverse spinel oxide was synthesized using a microwave-assisted hydrothermal method. 0.0025 M of $Cu(CH_3)COO_2.H_2O$, 0.045 M of $NiCl_2{\cdot}6H_2O$, 0.1 M of $CoCl_2{\cdot}6H_2O$, and 0.3 M of urea ($CO(NH_2)_2$) were added to 50 mL of double-distilled water. The obtained solution was moved to a Teflon-lined autoclave, sealed and subjected to microwave treatment at a temperature of 120 °C for 30 min. The autoclave was cooled down naturally to room temperature, and the precipitates were gathered and repeatedly centrifuged using ethanol and double-distilled water. Pure $NiCo_2O_4$ inverse spinel oxide is synthesized using a similar method as aforementioned, employing 0.05 M $NiCl_2{\cdot}6H_2O$, 0.1 M $CoCl_2{\cdot}6H_2O$, and 0.3 M urea ($CO(NH_2)_2$) for comparison. All the samples were dried in an oven at 60 °C for 24 h, followed by calcination for 2 h at 350 °C in a muffle furnace. Fig. S1 shows the schematic representation of the preparation of the CNCO10 sample. The obtained samples were labelled as NCO and CNCO10 for pure and 10% Cu-doped samples, respectively.

2.2. Material characterization

The Cu-doped $NiCo_2O_4$ samples were characterized using various techniques. The XRD patterns of the samples were recorded using a Bruker D8 Advance diffractometer with Cu K_α radiation (voltage: 45 kV, current: 30 mA) in a 2θ range of 10°-80° with a step size of 0.040°. Inductively Coupled Plasma (ICP) mass spectroscopy (Analytik Jena model Plasma Quant MS) was used to record the spectrum to quantify each element present in the samples. Nitrogen adsorption−desorption isotherms were recorded using the BET [Quantachrome®ASiQwin™] with a degassing temperature of 250 °C for 10 h to determine the surface area and porosity of the samples. The morphology of the prepared samples was obtained by micrograph analysis using a Scanning Electron Microscope (Carl Zeiss EVO 18 Research), operating at an accelerating voltage of 15 kV and working distance of 10.6 mm. Energy-dispersive X-ray spectroscopy (EDX) was performed using a Thermo Scientific™ Helios™ UXe DualBeam G4 system equipped with an EDX detector and focused ion beam (FIB), operated at 15 kV and a working distance of 4.0 mm. Here, FIB played a paramount role in facilely performing the cross-sectional imaging of the aggregated nanoparticles, as performed in our previous works [33]. PHI 5400 ESCA system (Supplied by Physical Electronics, Inc.) was used for XPS analysis, with a pass energy of 89.45 eV during the measurement of full survey scans and 71.55 eV for measuring the high-resolution, to study the different valence states of each element present on the surface of the pure and Cu-doped $NiCo_2O_4$ samples. All the XPS spectra were recorded using a non-monochromatized Aluminium (Al) K_α X-ray ($h\nu$ =1486.7 eV) source operated at 200 W power with 13.5 kV accelerating voltage under the pressure of 10^{-9} mbar. All the XPS spectra were analysed using MultiPak v. 8.0 software, provided by Physical Electronics Inc.

2.3. Fabrication of lithium-ion cells and their electrochemical characterization

CR-2032-type coin cells were fabricated inside an argon-filled glovebox. The working electrode was prepared as follows: The as-

synthesized NCO or CNCO10 nanomaterials, Polyvinylidene fluoride (PVDF) as binder and Super-C carbon as a conductive material (weight ratio of 8:1:1), were mixed in a *N*-methyl-2-pyrrolidene (NMP) solution to form a slurry, which was pasted on a copper foil and dried in an oven at 80 °C for 12 h and cut it into a circular disc of 8 mm. The counter electrode was made of pure lithium foil. The electrolyte solution was 1 M $LiPF_6$ in ethylene carbonate (EC)/dimethyl carbonate (DMC) (1:1 by volume), and the separator was glass microfiber filter paper (Whatman). Electrochemical studies were carried out on the fabricated CR 2032 cells using a Biologic BCS-810 battery cycler. Cyclic voltammograms were recorded at a scan rate of 0.1 mV s^{-1} in the potential range of 0.0–3.0 V. Galvanostatic charge-discharge curves were recorded at different current densities within a voltage range of 0.0–3.0 V. Electrochemical Impedance Spectra were recorded in the range of 10 kHz to 1 Hz, both before and after 100 cycles.

3. Results and discussion

3.1. Structural and morphological characterization of Cu doped $NiCo_2O_4$

The XRD patterns of NCO and CNCO10 samples, along with ICDD data [ICDD data no. 98–000-8294], are given in Fig. 1(i). The diffractograms of NCO and CNC10 samples were compared with ICDD data and the observed diffraction peaks at 18.9°, 31.2°, 36.7°, 38.4°, 44.8°, 48.9°, 55.4°, 59.1° and 65° were respectively assigned to (111), (220), (311), (222), (400), (422), (511), (440) and (533) planes [34]. The observed XRD pattern confirms the formation of phase-pure face-centered inverse spinel $NiCo_2O_4$ structure with a space group of Fd-3 m [32]. From Fig. 1(i), only a negligible shift was observed after Cu incorporation. An average crystallite size [D] and lattice parameter (a) of the prepared samples is calculated using Williamson-Hall (W–H) and Nelson -Riley plots, and the values are tabulated in **Table S1** [35].

From **Table S1**, the calculated average crystallite size of both NCO and CNCO10 samples is in the nanometer range, which confirms the formation of nanosized structures. The observed increase in the crystallite size of CNCO10 with Cu doping concentration can be due to the expansion in the lattice created by the introduction of the higher ionic radius Cu ions in the Ni sites of $NiCo_2O_4$ [36]. Also, the obtained lattice parameter remains nearly unchanged, suggesting that Cu ions are incorporated into the spinel lattice without causing significant structural distortion due to comparable ionic radii of Cu^{2+} (0.73 Å) and Ni^{2+} (0.69 Å) [37].

Fig. 1**(ii)** shows nitrogen adsorption–desorption isotherms of NCO and CNCO10 samples. From Fig. 1**(ii)**, the observed shape of the hysteresis patterns is similar for both samples, which are compared with IUPAC classifications of physisorption isotherms and identified as type IV, H3 type hysteresis with open-wedge pores [38]. **Fig. S2 (a) and (b)** shows the pore distribution curves of the NCO and CNCO10 samples calculated using the Barrett–Joyner–Halenda [BJH] method. From the pore size distribution curves, the effective pore width is distributed in the range of 2 to 50 nm with a sharp peak at 2.5 and 7.8 nm for NCO and 2.5, 4.3, and 8.2 nm for CNCO10, confirming the mesoporous nature of both samples. **Table 1** shows the surface area and pore volume of NCO and CNCO10 samples. From **Table 1**, the CNCO10 sample exhibits a higher surface area and pore volume compared to NCO, due to the unique nano-cube-like structure agglomerated to form porous nanorod-like morphology, which can provide additional active sites for lithium-ion storage and thereby enhance its electrochemical performance.

Fig. S3 shows the XPS survey spectrum of NCO and CNCO10 samples. From **Fig. S3**, the XPS survey spectrum of the NCO sample displays the characteristic peaks of Ni, Co, O and C elements, confirming their presence in the surface of the sample. In the case of CNCO10, along with the above elements, the photoelectron peaks of copper in the binding energy region of 932 eV become highly apparent. The Fig. 1**(iii) (a–d)** displays high-resolution XPS spectra of elements observed in CNCO10. Prior to high-resolution data analysis in this work, charge correction was achieved by referencing the main adventitious hydrocarbon (C—C) peak to 284.8 eV (**Fig. S4**).

The chemistry fitting technique of XPS analysis, where a single peak is indexed to a single oxidation state, does not represent the actual oxidation states in transition metals. "In a recent study, Hughes et al. highlighted the invalidity of employing a chemistry fitting approach (fitting each peak to a distinctive oxidation state) for transition metals and rare earth elements. Based on their recommendations, we presented the experimental data as obtained and did not deconvolute them to determine the multiple oxidation states" [39]. This explains the reason why we did not fit the high-resolution Ni 2p, Co 2p, and Cu 2p spectra in this study. However, based on the overall shape of the spectra (Co 2p in Fig. 1**(iii) b**), coupled with relatively low intensity for the satellite peaks and $\Delta = 15.1$ eV ($\Delta = E\left(2p_{3/2}\right) - E\left(2p_{1/2}\right)$) confirms that the mixed valence states of Co^{2+} and Co^{3+} are present in our sample [40]. Likewise, for the Ni 2p spectrum, the characteristic peak positions of Ni $2p_{3/2}$ and Ni $2p_{1/2}$ at 854.9 and 872.9 eV, respectively, indicate the presence of the Ni^{2+} oxidation state, which is especially occupied at octahedral sites of the material according to the crystal structure [40]. By comparison to the literature, the broad peaks of the Cu $2p_{3/2}$ and Cu $2p_{1/2}$ spin orbits with the characteristic presence of satellite peaks indicate that mixed valence states Cu^{2+} and Cu^{+} are present in the CNCO 10 sample [41].

In the case of the O 1 s spectrum of the CNCO10 sample, the chemistry fitting becomes valid; thus, the high intensity deconvoluted fitted peak at the binding energy of 529.16 eV is attributed to the lattice oxygen, indicating the oxygen is bonded to metal atoms. The second broad fitted peak at 531 eV could be assigned to the hydroxyl group attached to metal atoms. Finally, the small peak at 532.8 eV corresponds to chemically and/or physically bonded water molecules on the surface of the sample [42–44].

Table 2 shows the ICP-MS data of the NCO and CNCO10 samples. A small deviation from the expected stoichiometric ratio is observed in the evaluated stoichiometric ratio from ICP data. The observed small deviation in the stochiometric ratio can be due to experimental or evaluation error during sample measurement or the synthesis procedure. From Table 2, the presence of Cu in the $NiCo_2O_4$ matrix for the CNCO10 sample is confirmed.

Fig. 2 shows the SEM images of pure and Cu doped $NiCo_2O_4$ samples. From Fig. 2 **(a),** the morphology of the NCO is observed to be a nanoflake-like structure. After copper doping, the CNCO10 samples show a nano-cube-like structure agglomerated to form porous nanorods [Fig. 2 **(b)**]. This structural change from nanoflakes to nano-cubes can be due to the influence of Cu doping in the host matrix of $NiCo_2O_4$ [45]. In the case of NCO, the individual NCO particles are nucleated and grown as irregular crystals, and all these particles are aggregated to form a flake-like structure. The presence of Cu ions in the reaction mixture influences the nucleation growth rate of $NiCo_2O_4$ nanoparticles. As a result, it forms well-defined nano-cubes. The adsorption of Cu ions on $NiCo_2O_4$ nanoparticles influences the Van der Waals forces and electrostatic interactions, leading to self-aggregation of nano-cubes to form nanorod-like structures, in contrast to nanoflake-like structures **[37,46]**. A cross-sectional SEM micrograph and elemental mapping of the CNCO10 sample are presented in Fig. 2(c) and (d), respectively, which confirms the presence of Cu inside the nanostructure.

3.2. Electrochemical characterization of Cu doped $NiCo_2O_4$

Fig. 3(i) **(a) and (b)** show the cyclic voltammograms (CV) of NCO and CNCO10 samples. From Fig. 3(i) **(a) and (b)**, in the first cycle, the observed irreversible reduction peak at 0.80 V corresponds to the reduction of $NiCo_2O_4$ to metallic cobalt and nickel, and the formation of amorphous Li_2O and the generation of a solid-electrolyte interface (SEI) layer [47]. The observed two oxidation peaks at 1.4 V and 2.1 V are attributed to the oxidation reaction of Ni^0 and Co^0 to form Ni^{2+} and

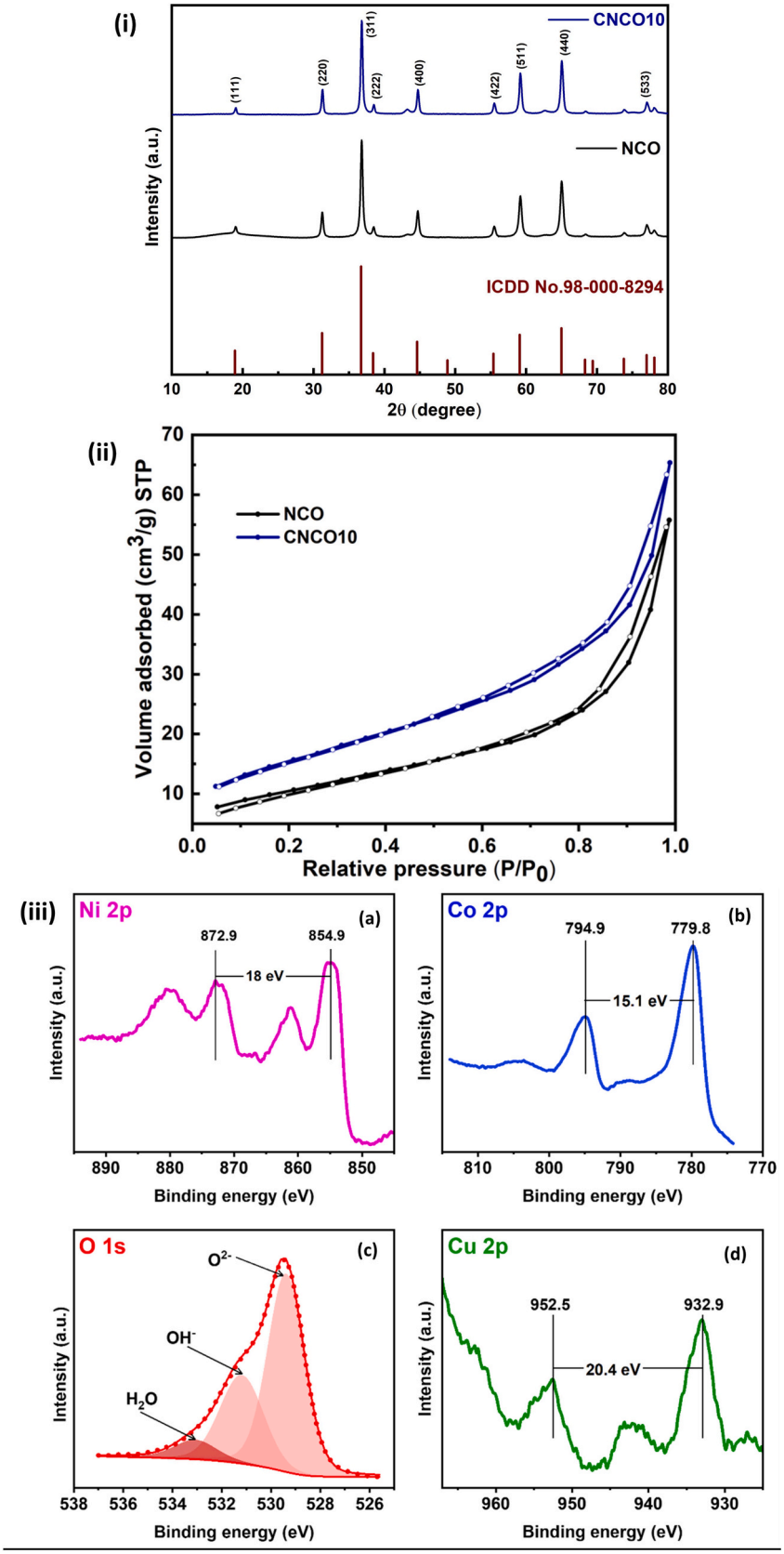

Fig. 1. (i) XRD patterns of ICDD data (brown line), NCO (black line), and CNCO10 (blue line), (ii) Nitrogen adsorption-desorption isotherms of NCO and CNCO10, and (iii) XPS analysis of (a) Ni 2p, (b) Co 2p, (c) O 1 s, and (d) Cu 2p high-resolution spectra of CNCO10. (For interpretation of the references to colour in this figure legend, the reader is referred to the web version of this article.)

Table 1
Surface area and pore volume of Cu doped $NiCo_2O_4$.

Sample	Specific surface area (m^2/g)	Pore volume (cc/g)
NCO	38.8	0.08
CNCO10	59.4	0.10

Table 2
ICP data of the prepared NCO and CNCO10 sample.

Sample	Ni (M)	Co (M)	Cu (M)	Theoretical ratio (Cu:Ni:Co)	Experimental ratio (Cu:Ni:Co)
NCO	4.23	9.37	–	0:1:2	0:1:2.2
CNCO10	3.86	9.25	0.34	0.1:0.9:2	0.07:0.90:2.15

Co^{3+}, respectively [48]. There is no shift in oxidation peaks in the second cycle, while the reduction peak is shifted to a higher potential (1.12 V), corresponding to two reversible reactions (Eqs. 2 & 3), implying that the reduction reaction happens facilely in the following cycles. It is evident from the CV curves that copper doping has a major impact on the current value. The CNCO10 electrode shows a higher current value (1.2 mA) when compared to NCO (0.9 mA) for the initial cycle, which can be due to improved conductivity after Cu doping, and the CV curves tend to overlap with cycles when compared to NCO electrodes. These sharp and overlapped curves indicate the enhanced electron transfer and higher reversible capacity of the CNCO10 electrode material.

The above electrochemical reaction process of NCO can be described by the following equations [49].

$$NiCo_2O_4 + 8Li^+ + 8e^- \rightarrow Ni + 2Co + 4Li_2O \quad (1)$$

$$Ni + Li_2O \leftrightarrow NiO + 2Li^+ + 2e^- \quad (2)$$

$$Co + Li_2O \leftrightarrow CoO + 2Li + + 2e^- \quad (3)$$

$$CoO + 1/3Li_2O \leftrightarrow 1/3Co_3O_4 + 2/3Li^+ + 2/3e^- \quad (4)$$

Fig. 3**(ii) (a) and (b)** represent the charge-discharge profiles of selected cycles for NCO and CNCO10, respectively. The plateau region of the first discharge curve is lower than that for other cycles in the discharge curves of both NCO and CNCO10, which corresponds to the irreversible reaction of NCO as in Eq. (1), which is in accordance with the previously discussed CV results. The observed initial discharge capacity of NCO and CNCO10 is found to be 1432 mAh g^{-1} and 1572 mAh g^{-1}, respectively, and is found to be higher than the theoretically

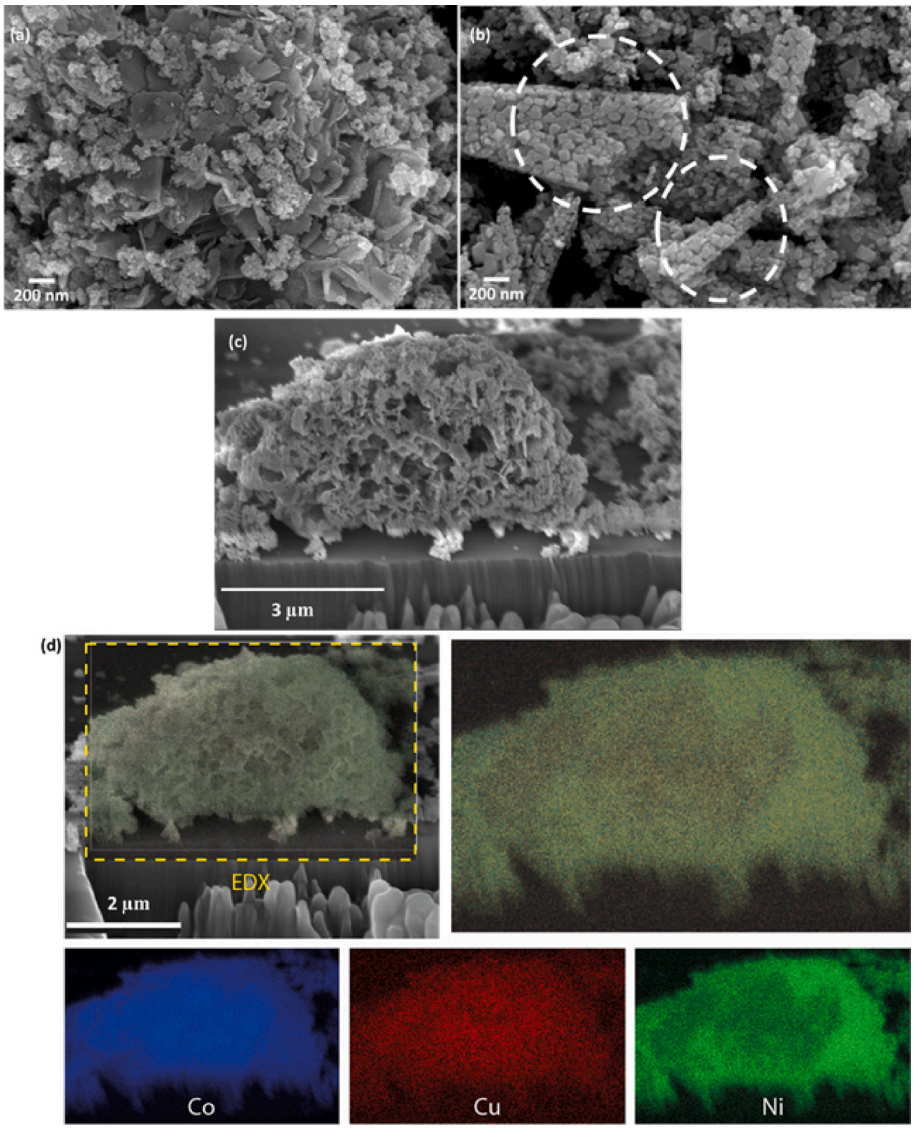

Fig. 2. SEM images of (a) NCO, (b) CNCO10, (c) cross-sectional SEM image of CNCO10, and (d) cross-sectional elemental mapping of the CNCO10 sample.

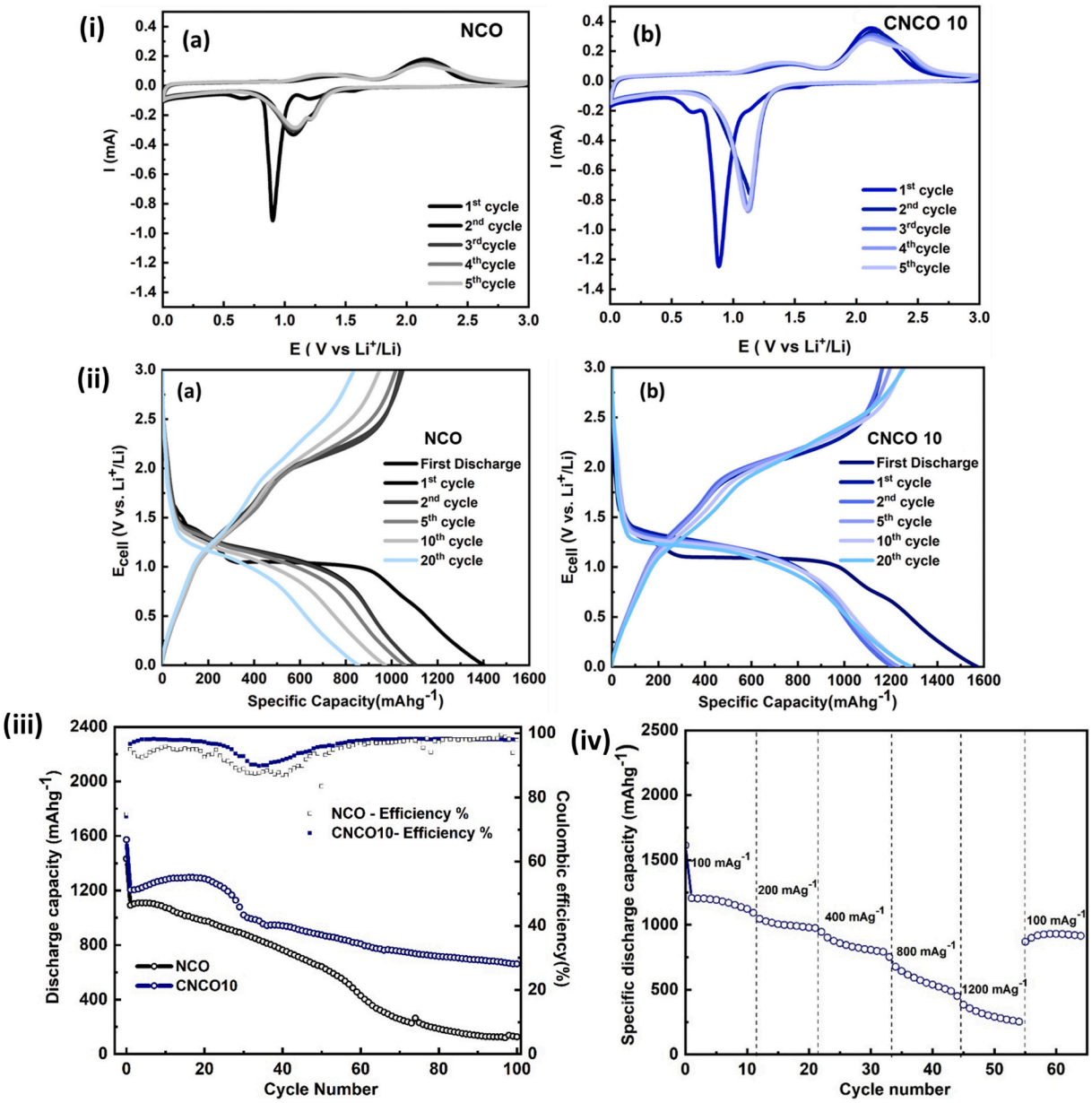

Fig. 3. (i) Cyclic Voltammogram of (a) NCO and (b) CNCO10, (ii) Charge-discharge cycles of (a) NCO and (b) CNCO10 for the first 20 cycles, (iii) Discharge capacity and coulombic efficiency of NCO and CNCO10 at a current density of 100 mA g^{-1} up to 100 cycles and (iv) Rate performance of the CNCO10 electrode.

calculated specific capacity value of $NiCo_2O_4$ of 890 mAh g^{-1}. This irreversible residual capacity, when compared to the theoretical capacity, indicates the formation of a Solid Electrolyte Interface (SEI) by electrolyte degradation [50]. The first initial specific charge capacity NCO and CNCO10 is found to be 1039 mAh g^{-1} and 1163 mAh g^{-1}. Thus, the increased specific capacity of CNCO10 over NCO can be due to improved electronic conductivity after introducing copper atoms to the $NiCo_2O_4$ matrix.

Fig. 3**(iii)** shows the discharge capacity and coulombic efficiency for 100 cycles of NCO and CNCO10 samples, respectively. From Fig. 3**(iii),** it is observed that the NCO electrodes' specific capacity is decreasing with cycling and reached a value of 127 mAh g^{-1} with a coulombic efficiency of 97% after 100 cycles. For CNCO10 electrodes, the specific discharge capacity of 1286 mAh g^{-1} is maintained up to 30 cycles and then stabilizes at 662 mAh g^{-1} with a coulombic efficiency of 98% after 100 cycles.

Fig. S5 shows the charge-discharge cycles of CNCO5 and CNCO20 [5% and 20% Cu doping in $NiCo_2O_4$]. From Fig. S7, both 5% and 20% of Cu doping show an initial discharge capacity of 1268.3 and 1533.4 mAh g^{-1}. But after 20 cycles, CNCO5 shows a fast capacity fading similar to NCO electrodes. On the other hand, CNC020 electrodes show a better cyclic performance than NCO and CNCO5; their performance is still inferior to that achieved with the CNCO10 electrode. This inferior performance of the CNCO20 electrode likely arises from Cu ion agglomeration in the NCO host matrix due to its large concentration, which suggests that a 10% Cu doping is the optimally tuned concentration.

The abnormal decline in the cyclic performance and coulombic efficiency of NCO and CNCO10 after 30 cycles may be due to multiple factors including structural changes during continuous charge-discharge cycles, irreversible Li^+ trapping and formation of unstable Solid Electrolyte Interphase (SEI) layer that forms on the $NiCo_2O_4$ electrode, leading to discharge capacity fading during cycling. Once the SEI layer stabilizes and its growth slows, the coulombic efficiency typically increases and reaches a steady value [51].

The major reasons for the capacity drop in the NCO electrode when compared to CNCO10 are the poor conductivity of NCO and volume

expansion that leads to its pulverization during cycling. The addition of Cu improves the conductivity of $NiCo_2O_4$; also, the Cu acts as an inactive material, which reduces the volume expansion, resulting in improved electrochemical performance of 10% Cu doped $NiCo_2O_4$ as an anode material for lithium-ion batteries.

Fig. 3**(iv)** shows the rate performance for the CNCO10 electrode at various current densities from 100 to 1200 mAg^{-1}. The discharge capacity decreases from 1161 mAh g^{-1} to 1068 mAh g^{-1} after 11 cycles at a current density of 100 mAg^{-1}. The discharge capacities of the CNCO10 electrode at the current density of 100, 200, 400, 800, and 1200 mAg^{-1} are found to be 1068, 948, 742, 443, and 253 mAh g^{-1}, respectively, in the 11th, 21st, 32nd, 43rd, and 54th cycles. A good rate performance of 896 mAh g^{-1} is recovered after the current density is returned to 100 mAg^{-1}. This reversible capacity retention and relatively high specific capacity with good rate performance of CNCO10 can be due to the introduction of copper to the $NiCo_2O_4$ host matrix, where copper may act as an inactive material and help in reducing the volume expansion occurring during the charge-discharge process.

Fig. 4(a) and (b) display the Nyquist plots of the NCO and CNCO10 electrodes before cycling and after 100 cycles, over a frequency range of 10 kHz to 1 Hz. The obtained curves are fitted with a suitable electrical equivalent circuit, as given in the Figure inset. Table 3 shows impedance parameters of the developed NCO and CNCO10 electrodes. The fitting of the Randles circuit for the EIS data gave a very low χ^2 value (in the range of 10^{-3}). From Table 3, the charge-transfer resistance (R_{ct}) refers to the resistance at the electrode-electrolyte interface, which is the semicircle in the middle frequency range of the Nyquist plot. Warburg impedance (W) shows the diffusional behaviour of Li^+ ions in the electrode, which is the inclined line in the low frequency region. R_s represents the ohmic resistance of the electrolyte, the intrinsic resistance of the active material, and contact resistance at the electrode/current collector interface. The constant phase element (CPE_{dl}) indicates double-layer capacitance at the electrode/electrolyte boundary, indicating a deviation from ideal capacitive behaviour, attributed to the material's porous structure and

Table 3
Comparison of EIS parameters of the developed anodes of NCO and CNCO10 before cycling.

Electrode material	R_s (Ω)	R_{ct} (Ω)	CPE_{dl} (μF cm^{-2})	R_{SEI} (Ω)	Warburg factor ($\Omega s^{1/2}$)	χ^2
Before cycling						
NCO	6.9	144.9	47.4	–	139.8	9.64×10^{-3}
CNCO10	3.2	62	82.7	–	137.2	7.64×10^{-3}
After cycling						
NCO	40.7	62.6	44.4	23.5	1171.1	6.13×10^{-3}
CNCO10	7.2	106.6	147.6	3.9	699.1	2.83×10^{-3}

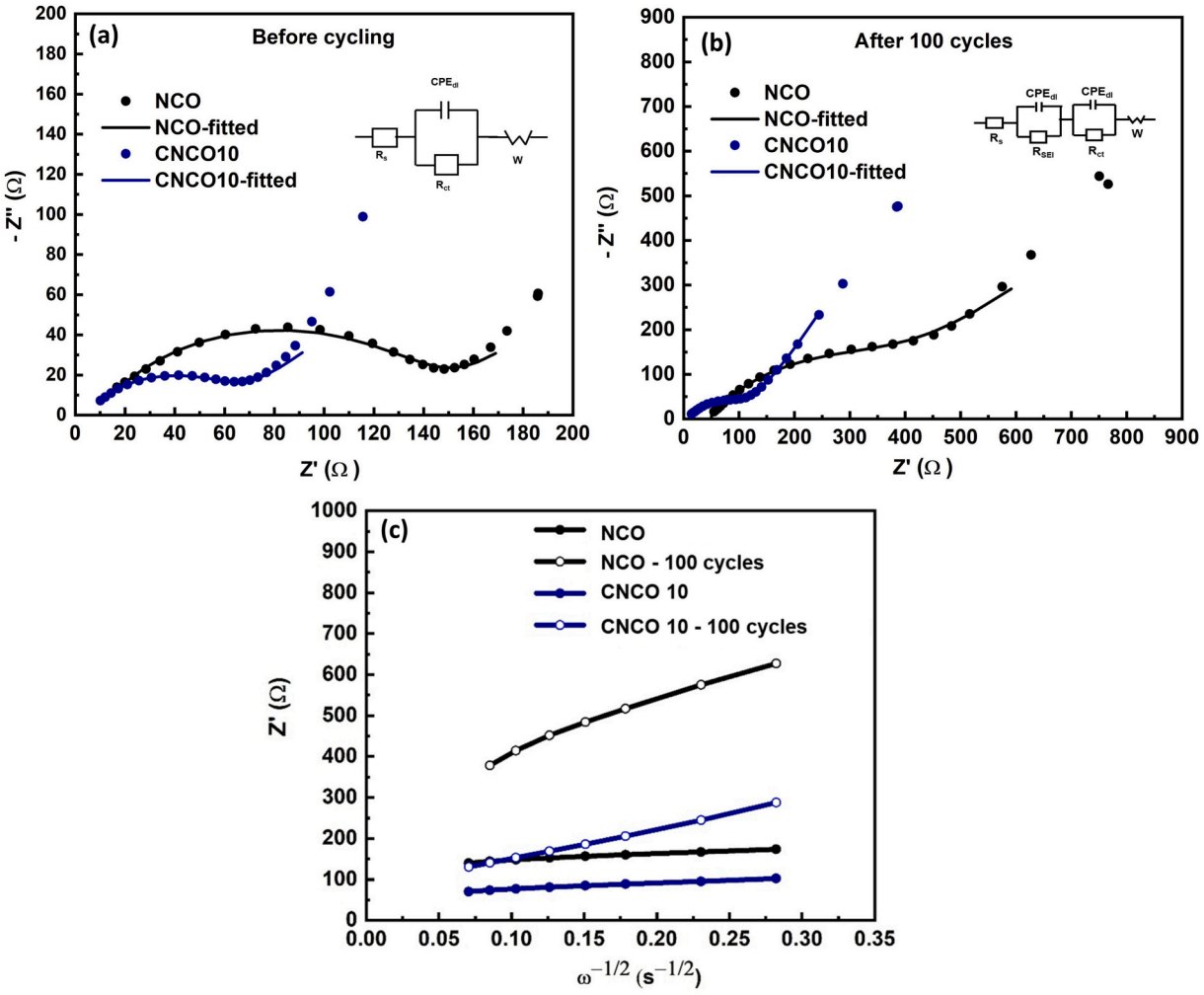

Fig. 4. EIS spectra of (a) before and (b) after cycling and fitted with a suitable equivalent circuit in the inset, and (c) Real parts of the complex impedance Re(Z) vs. $\omega^{-1/2}$.

surface roughness. R_{SEI} is the resistance due to the SEI layer formation [12].

From Table 3, it was observed that ohmic resistance (R_s) increased after 100 cycles due to electrolyte degradation. CNCO10 shows the lowest charge-transfer resistance of 62 Ω when compared to NCO, which has a charge-transfer resistance of 144.9 Ω. After 100 cycles, the R_{ct} value increases for both NCO (626.6 Ω) and CNCO 10 (106.6 Ω) electrodes. The Cu doping decreases the charge-transfer resistance of $NiCo_2O_4$ electrode, facilitating faster interfacial charge-transfer kinetics during the lithiation/delithiation process resulting in enhanced electrochemical performance. Post-cycling analysis reveals that after 100 cycles, CNCO10 develops an SEI layer with lower resistance than for the NCO electrode.

The diffusion coefficients (D_{Li}) for Li-ion kinetics of the cells can also be determined based on the EIS profiles in the low-frequency region [52].

$$\sigma = \frac{RT}{n^2F^2A\sqrt{2}}\left(\frac{1}{C_{Li}D_{Li}^{\frac{1}{2}}}\right) \quad (5)$$

where R, universal gas constant

F, Faraday constant

T, absolute temperature

A, electrode surface area

n, number of electrons transferred per molecule

C_{Li} , molar concentration of active material

σ, Warburg factor.

The Warburg factor is calculated by determining the slope obtained from the linear fitting of Z_{re} to $\omega^{-1/2}$ plots [53,54]. Fig. 4(c) shows the obtained slope of NCO and CNCO10 materials. From Eq. 5, the Warburg factor (σ) has an inverse relation with the diffusion coefficient D_{Li}. From Table 3, the CNCO10 electrode has a lower Warburg factor of 699.1 $\Omega s^{-1/2}$ than NCO (137.2 $\Omega s^{-1/2}$) after 100 cycles, suggesting a rapid diffusion of lithium-ions into the CNCO10 electrode.

The above results show that the introduction of copper to the $NiCo_2O_4$ host matrix has a significant effect on electrochemical properties. The introduction of copper to the $NiCo_2O_4$ lattice increases the electronic conductivity and surface area of $NiCo_2O_4$, which provides more active sites for redox reactions to happen [32]. Also, the Cu acts as an inactive material, which restrains the volume expansion during the reaction, resulting in enhanced cyclic performance of CNCO10 over the NCO electrode. Fig. 5 shows the schematic diagram of the mechanism of Cu doping on $NiCo_2O_4$. Therefore, the synergetic effect of Cu^{2+}, Ni^{2+}/Ni^{3+}, and $Co^{2+/}Co^{3+}$ in CNCO10 results in improved electrochemical performance as an anodic material for lithium-ion batteries.

4. Conclusions

Development of porous nanorod-like Cu-doped $NiCo_2O_4$ (CNCO10) ternary metal oxide was successfully carried out using a microwave-assisted hydrothermal method. The doping was performed such that the resultant compound maintained a crystalline structure with partial substitution of Cu^{+}/Cu^{2+} ions in the $NiCo_2O_4$ matrix, with no impurity phases as confirmed by XRD analysis. The morphological studies confirm that Cu doping increases the surface area of $NiCo_2O_4$ by 34.7% when compared to pure $NiCo_2O_4$. The Cu doping increases the conductivity of the host matrix, thus improving electrochemical performance, which is validated by a relatively high initial specific capacity of 1572 mAh g^{-1} for 10% Cu doped $NiCo_2O_4$, while the $NiCo_2O_4$ electrode has an initial discharge specific capacity of 1432 mAh g^{-1}. Introduction of Cu in $NiCo_2O_4$ also controls the volume expansion during the continuous charge-discharge process, resulting in a better cyclic stability when compared to pure $NiCo_2O_4$. The improved electrochemical performance was also validated through EIS measurements, which indicated a lower transfer resistance upon Cu doping compared to that for pure $NiCo_2O_4$. From this study, the Cu doped $NiCo_2O_4$ outperformed pure $NiCo_2O_4$ material, which makes Cu doping strategy a promising method for the development of a potential anode material with high cycle stability for lithium storage and for other battery applications like Zn, Na, etc. Table 4 shows the comparison of different literature studies on the electrochemical performance of cationic doping on the metal oxides in different battery chemistries with our present work.

CRediT authorship contribution statement

Durga S. Nair: Writing – review & editing, Writing – original draft, Visualization, Validation, Methodology, Investigation, Formal analysis, Data curation, Conceptualization. **Reshma S. Babu:** Writing – review & editing, Formal analysis, Data curation. **Bharath Chandran:** Writing – review & editing, Data curation, Conceptualization. **Prasad Gonugunta:** Writing – review & editing, Supervision, Formal analysis, Data curation. **Thamayanthi Panneerselvam:** Resources, Formal analysis, Data curation. **Ramaswamy Murugan:** Resources. **Harish Kumar:** Visualization, Validation, Supervision, Resources. **Ruud Hendrikx:** Formal analysis, Data curation. **Arjan Cornet:** Investigation, Formal analysis, Data curation. **Arjan Mol:** Visualization, Validation, Resources, Conceptualization. **N. Satyanarayana:** Writing – review & editing, Visualization, Validation, Supervision, Resources, Project administration, Conceptualization. **Prasaanth Ravi Anusuyadevi:** Writing – review & editing, Visualization, Validation, Supervision, Resources, Methodology, Formal analysis, Data curation, Conceptualization.

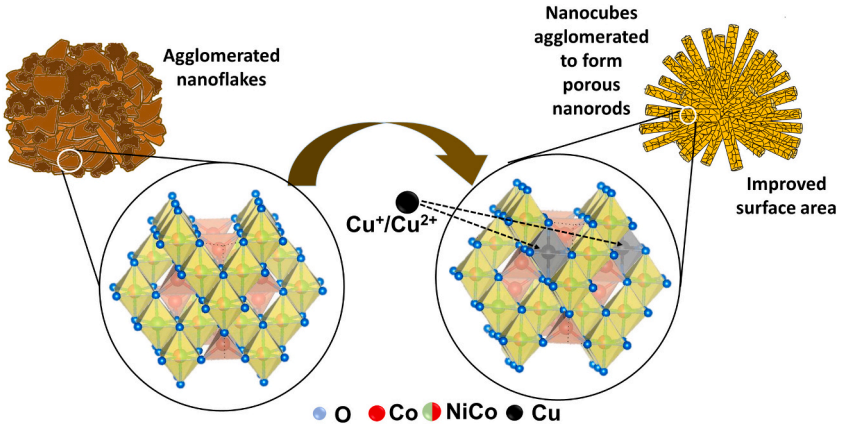

Fig. 5. Schematic diagram showing the mechanism of Cu doping on $NiCo_2O_4$.

Table 4
Comparison table showing the electrochemical performance of cationic doping on metal oxides in different battery chemistries with the present work.

Anode material	Battery chemistry	Specific capacity ($mAhg^{-1}$)	No. of cycles	Reference
Mn-doped $NiCo_2O_4$	Lithium-ion Batteries	945 @2 A g^{-1}	500	[30]
NiCo-NiCo2O4@C nanotubes	Lithium-ion Batteries	616.2 @ 0.1 Ag^{-1}	1000	[54]
Cu doped δ-MnO_2	Aqueous Zn-ion batteries	296.8 @100 mAg^{-1}	120	[55]
Cu-doped Co_3O_4	Lithium -ion Batteries	1293 @100 mAg^{-1}	300	[56]
Cu-doped Co_3O_4	Sodium -ion Batteries	522 @100 mAg^{-1}	300	[56]
Cu-doped Co_3O_4	Potassium ion Batteries	331 @100 mAg^{-1}	300	[56]
Cu-Fe_2O_3	Lithium -ion Batteries	239.4 @100 mAg^{-1}	200	[57]
Cu-Fe_2O_3	Sodium ion Batteries	49 @100 mAg^{-1}	200	[57]
Mo-doped $NiCo_2O_4$	Lithium-ion Batteries	485 @0.3Ag^{-1}	270	[58]
P-doped $NiCo_2O_4$ microspheres	Lithium-ion Batteries	470 @0.5 A g^{-1}	100	[59]
Mo-doped $NiCo_2O_4$	Lithium-ion Batteries	1360 @ 0.3 A g^{-1}	100	[60]
F-$Fe_xMn_{1-x}MoO_4$/ graphene	Lithium-ion Batteries	780 @0.1C	100	[61]
Cu doped $NiCo_2O_4$	Lithium-ion Batteries	662 @ 100 mAg^{-1}	100	Present work

Declaration of competing interest

The authors declare that they have no known competing financial interests or personal relationships that could have appeared to influence the work reported in this paper.

Acknowledgements

D.S.N. is grateful to the Central Laboratory for Instrumentation and Facilitation (CLIF), University of Kerala for utilizing the characterization facilities. R.S·B grateful to CSIR, Govt of India, for CSIRSRF Fellowship (No. 09/559(0158)/2020-EMR-I). N.S. acknowledges UGC, Govt of India, for awarding UGCBSR Faculty Fellowship (No. F.18-1/2011 (BSR), Date: 07-03-2019).

Appendix A. Supplementary data

Supplementary data to this article can be found online at https://doi.org/10.1016/j.rechem.2026.103752.

Data availability

Data will be made available on request.

References

[1] T. Kim, W. Song, D.-Y. Son, L.K. Ono, Y. Qi, Lithium-ion batteries: outlook on present, future, and hybridized technologies, J. Mater. Chem. A 7 (7) (2019) 2942–2964, https://doi.org/10.1039/C8TA10513H.
[2] X. Xu, X. Han, L. Lu, F. Wang, M. Yang, X. Liu, Y. Wu, S. Tang, Y. Hou, J. Hou, C. Yu, M. Ouyang, Challenges and opportunities toward long-life lithium-ion batteries, J. Power Sources 603 (2024) 234445, https://doi.org/10.1016/j.jpowsour.2024.234445.
[3] N. Gopalakrishnan, N.M. Suntharam, S. Bashir, B. Vengadaesvaran, N.A. Rahim, Y. Gunasekaran, S. Ramesh, K. Ramesh, A. Uttran, Advancements in cathode materials for Lithium-ion batteries: an overview of future prospects, Ionics (Kiel) 31 (2) (2025) 1153–1180, https://doi.org/10.1007/s11581-024-06030-1.
[4] P.U. Nzereogu, A.D. Omah, F.I. Ezema, E.I. Iwuoha, A.C. Nwanya, Anode materials for lithium-ion batteries: a review, Appl. Surf. Sci. Adv. 9 (2022) 100233, https://doi.org/10.1016/j.apsadv.2022.100233.
[5] C. Wang, C. Yang, Z. Zheng, Toward practical high-energy and high-power lithium battery anodes: present and future, Adv. Sci. 9 (9) (2022) 2105213, https://doi.org/10.1002/advs.202105213.
[6] Z. Xiao, R. Wang, D. Jiang, Z. Qian, Y. Li, K. Yang, Y. Sun, Z. Zeng, F. Wu, Recent developments of two-dimensional anode materials and their composites in lithium-ion batteries, ACS Appl. Energy Mater. 4 (8) (2021) 7440–7461, https://doi.org/10.1021/acsaem.1c01259.
[7] W. Zhao, C. Zhao, H. Wu, L. Li, C. Zhang, Progress, challenge and perspective of graphite-based anode materials for lithium batteries: a review, J. Energy Storage 81 (2024) 110409, https://doi.org/10.1016/j.est.2023.110409.
[8] T. Insinna, E.N. Bassey, K. Märker, A. Collauto, A.-L. Barra, C.P. Grey, Graphite anodes for Li-ion batteries: an electron paramagnetic resonance investigation, Chem. Mater. 35 (14) (2023) 5497–5511, https://doi.org/10.1021/acs.chemmater.3c00860.
[9] G.F.I. Toki, M.K. Hossain, W.U. Rehman, R.Z.A. Manj, L. Wang, J. Yang, Recent progress and challenges in silicon-based anode materials for lithium-ion batteries, Ind. Chem. Mater. 2 (2) (2024) 226–269, https://doi.org/10.1039/D3IM00115F.
[10] H. Wang, S. Chen, C. Fu, Y. Ding, G. Liu, Y. Cao, Z. Chen, Recent advances in conversion-type electrode materials for post lithium-ion batteries, ACS Mater. Lett. 3 (7) (2021) 956–977, https://doi.org/10.1021/acsmaterialslett.1c00043.
[11] B. Chandran, R.S. Babu, P. Gonugunta, O. Padmaraj, T. Panneerselvam, R. Murugan, G.R. Babu, R. Hendrikx, P. Taheri, A. Mol, N. Satyanarayana, P. R. Anusuyadevi, Self-adaptive ZnMn2O4/α-MnO2 nanocomposite as an anode material for high-performance lithium-ion batteries, Appl. Surf. Sci. 712 (2025) 164175, https://doi.org/10.1016/j.apsusc.2025.164175.
[12] R.S. Babu, E. Madai, D.S. Nair, P. Gonugunta, S.M. Armaki, R. Hendrikx, T. Panneerselvam, R. Murugan, V.V.R.K. Kumar, P. Taheri, A. Mol, N. Satyanarayana, P.R. Anusuyadevi, Effect of synthesis conditions on morphology, surface chemistry and electrochemical performance of nickel ferrite nanoparticles for lithium-ion battery applications, J. Mater. Sci. Mater. Electron. 36 (14) (2025) 865, https://doi.org/10.1007/s10854-025-14886-w.
[13] J. Chen, N. Zhao, C. Tang, Y. Chen, Facile synthesis of Co3O4 with porous capsule–shaped structure and its lithium storage properties as anode materials for Li–ion batteries, Ceram. Int. 50 (17, Part B) (2024) 31567–31575, https://doi.org/10.1016/j.ceramint.2024.05.464.
[14] J. Liu, L. Dong, D. Chen, Y. Han, Y. Liang, M. Yang, J. Han, C. Yang, W. He, Metal oxides with distinctive valence states in an electron-rich matrix enable stable high-capacity anodes for Li ion batteries, Small Methods 4 (2) (2020), https://doi.org/10.1002/smtd.201900753.
[15] M.-C. Han, M. Zou, T.-F. Yi, F. Wei, Recent advances of ZnCo2O4-based anode materials for Li-ion batteries, Chem. Asian J. 18 (1) (2023) e202201034, https://doi.org/10.1002/asia.202201034.
[16] Y. Kang, H. Shi, Y.-H. Zhang, F.-N. Shi, High-performance ZnCo2O4 microsheets as an anode for lithium-ion batteries, Chem. Commun. 57 (82) (2021) 10723–10726, https://doi.org/10.1039/D1CC03769B.
[17] M. Dorri, C. Zamani, A. Babaei, Insights into temperature-induced evolution of spinel MnCo2O4 as anode material for Li-ion batteries with enhanced electrochemical performance, J. Alloys Compd. 941 (2023) 169034, https://doi.org/10.1016/j.jallcom.2023.169034.
[18] L. Zhu, F. Li, T. Yao, T. Liu, J. Wang, Y. Li, H. Lu, R. Qian, Y. Liu, H. Wang, Electrospun MnCo2O4 nanotubes as high-performance anode materials for lithium-ion batteries, Energy Fuel 34 (9) (2020) 11574–11580, https://doi.org/10.1021/acs.energyfuels.0c02302.
[19] X. Chen, J. Zhu, Y. Ding, X. Zuo, Synthesis of CuCo2O4 nanoparticles as an anode material with high performance for Lithium-ion batteries, J. Mater. Sci. Mater. Electron. 32 (14) (2021) 18765–18776, https://doi.org/10.1007/s10854-021-06395-3.
[20] Y. Yang, J. Gong, D. Cai, Y. Li, Y. Sun, W. Wang, C. Feng, Flexible synthesis of CuCo2O4 hexagonal nanocrystal by melting salt modified combustion method as high-performance anode materials for Lithium-ion batteries, J. Electroceram. 50 (3) (2023) 57–66, https://doi.org/10.1007/s10832-023-00305-1.
[21] G. Zheng, Z. Yuan, X. Huang, Y. Deng, X. Yu, M. Song, W. Zheng, Research on 3D network in-situ grown NiCo2O4 nanowire arrays construction and its energy storage performance, Solid State Ionics 401 (2023) 116359, https://doi.org/10.1016/j.ssi.2023.116359.
[22] T. Li, X. Li, Z. Wang, H. Guo, Y. Li, A novel NiCo2O4 anode morphology for Lithium-ion batteries, J. Mater. Chem. A 3 (22) (2015) 11970–11975, https://doi.org/10.1039/C5TA01928A.
[23] X. Han, X. Gui, T.-F. Yi, Y. Li, C. Yue, Recent Progress of NiCo2O4-based anodes for high-performance Lithium-ion batteries, Curr. Opin. Solid State Mater. Sci. 22 (4) (2018) 109–126, https://doi.org/10.1016/j.cossms.2018.05.005.
[24] R.-H. Qiao, B. Zhang, S.-Q. Wang, X.-M. Luo, G.-P. Zhang, Phosphate-modified $NiCo_2O_4$ @NiCoS heterointerface boosting electrochemical performance for supercapacitors, ACS Appl. Energy Mater. 7 (18) (2024) 8014–8024, https://doi.org/10.1021/acsaem.4c01735.
[25] V. Veeramani, R. Madhu, S.-M. Chen, M. Sivakumar, Flower-like nickel–cobalt oxide decorated dopamine-derived carbon nanocomposite for high performance supercapacitor applications, ACS Sustain. Chem. Eng. 4 (9) (2016) 5013–5020, https://doi.org/10.1021/acssuschemeng.6b01391.
[26] S. Yuvaraj, R.K. Selvan, Y.S. Lee, An overview of AB2O4- and A2BO4-structured negative electrodes for advanced Li-ion batteries, RSC Adv. 6 (26) (2016) 21448–21474, https://doi.org/10.1039/C5RA23503K.
[27] S. Maheshwaram, S. Gaddameedi, S.C. Chidurala, S. Katlakunta, V. N. Mudutanapalli, S. Daripalli, R.R. Butreddy, Structural and electrochemical properties of cu doped NiCo2O4 prepared by microwave hydrothermal method, Mater. Lett. 348 (2023) 134650, https://doi.org/10.1016/j.matlet.2023.134650.

[28] R. Li, H. Ke, C. Shi, Z. Long, Z. Dai, H. Qiao, K. Wang, Mesoporous RGO/NiCo2O4@carbon composite nanofibers derived from metal-organic framework compounds for lithium storage, Chem. Eng. J. 415 (2021) 128874, https://doi.org/10.1016/j.cej.2021.128874.
[29] Y.-T. Lu, Y.-J. Chien, C.-F. Liu, T.-H. You, C.-C. Hu, Active site-engineered bifunctional electrocatalysts of ternary spinel oxides, M0.1Ni0.9Co2O4 (M: Mn, Fe, Cu, Zn) for the air electrode of rechargeable zinc–air batteries, J. Mater. Chem. A 5 (39) (2017) 21016–21026, https://doi.org/10.1039/C7TA06302D.
[30] Z. Liang, H. Tu, Z. Kong, X. Yao, D. Xu, S. Liu, Y. Shao, Y. Wu, X. Hao, Urchin like inverse spinel manganese doped NiCo2O4 microspheres as high performances anode for Lithium-ion batteries, J. Colloid Interface Sci. 616 (2022) 509–519, https://doi.org/10.1016/j.jcis.2022.02.069.
[31] X. Han, L. Song, J. Ding, L. Hu, C. Xu, Y. Wang, Design and preparation of cu-doped NiCo2O4 nanosheets with intrinsic porosities for symmetric supercapacitors, Mater. Lett. 278 (2020) 128400, https://doi.org/10.1016/j.matlet.2020.128400.
[32] D.S. Nair, A. Anil, L. Elias, N. Satyanarayana, H.K. Holla, S.M.A. Shibli, Tuning of physicochemical and electronic characteristics of cu-doped NiCo2O4 ternary inverse spinel oxides for effective electrocatalytic hydrogen evolution reaction, Int. J. Hydrog. Energy 62 (2024) 162–171, https://doi.org/10.1016/j.ijhydene.2024.03.031.
[33] A.J. Cornet, A.M. Homborg, P.R. Anusuyadevi, L. 't Hoen-Velterop, J.M.C. Mol, Unravelling corrosion degradation of aged aircraft components protected by chromate-based coatings, Eng. Fail. Anal. 159 (2024) 108070, https://doi.org/10.1016/j.engfailanal.2024.108070.
[34] I. Ivanenko, A. Voronova, I. Astrelin, Y. Romanenko, Structural and catalytic properties of Ni–Co spinel and its composites, Bull. Mater. Sci. 42 (4) (2019) 172, https://doi.org/10.1007/s12034-019-1854-9.
[35] Somnath, K.M. Batoo, E.H. Raslan, S.F. Adil, I. Sharma, G. Kumar, Investigation of electrical, magnetic, and optical properties of silver-substituted magnesium–manganese ferrite nanoparticles, J. Mater. Sci. Mater. Electron. 31 (10) (2020) 7880–7888, https://doi.org/10.1007/s10854-020-03326-6.
[36] H. Park, B.H. Park, J. Choi, S. Kim, T. Kim, Y.-S. Youn, N. Son, J.H. Kim, M. Kang, Enhanced electrochemical properties and OER performances by Cu substitution in NiCo2O4 spinel structure, Nanomaterials 10 (9) (2020), https://doi.org/10.3390/nano10091727.
[37] S. Saleem, M. Irfan, M.Y. Naz, S. Shukrullah, M.A. Munir, M. Ayyaz, A.S. Alwadie, S. Legutko, J. Petrů, S. Rahman, Investigating the impact of Cu2+ doping on the morphological, structural, optical, and electrical properties of CoFe2O4 nanoparticles for use in electrical devices, Materials 15 (10) (2022) 3502, https://doi.org/10.3390/ma15103502.
[38] H. Zhang, J. Han, J. Xu, Y. Ling, X. Ou, Self-assembled NiCo2O4 microspheres for hybrid supercapacitor applications, J. Mater. Sci. 57 (9) (2022) 5566–5576, https://doi.org/10.1007/s10853-022-06967-6.
[39] A.E. Hughes, C.D. Easton, P.R. Anusuyadevi, T.J. Raeber, N.C. Wilson, A. Mol, Widespread erroneous analysis of the Fe 2p peak in X-ray photoelectron spectroscopy examination in corrosion studies, Corros. Sci. 257 (2025) 113357, https://doi.org/10.1016/j.corsci.2025.113357.
[40] J.-G. Kim, D.L. Pugmire, D. Battaglia, M.A. Langell, Analysis of the NiCo2O4 spinel surface with auger and X-ray photoelectron spectroscopy, Appl. Surf. Sci. 165 (1) (2000) 70–84, https://doi.org/10.1016/S0169-4332(00)00378-0.
[41] L. Martin, H. Martinez, D. Poinot, B. Pecquenard, F. Le Cras, Comprehensive X-ray photoelectron spectroscopy study of the conversion reaction mechanism of CuO in Lithiated thin film electrodes, J. Phys. Chem. C 117 (9) (2013) 4421–4430, https://doi.org/10.1021/jp3119633.
[42] Y. Ma, W. Shang, W. Yu, X. Chen, W. Xia, C. Wang, P. Tan, Synthesis of ultrasmall $NiCo_2O_4$ nanoparticle-decorated N-doped graphene nanosheets as an effective catalyst for Zn–air batteries, Energy Fuel 35 (17) (2021) 14188–14196, https://doi.org/10.1021/acs.energyfuels.1c02064.
[43] R. Zou, K. Xu, T. Wang, G. He, Q. Liu, X. Liu, Z. Zhang, J. Hu, Chain-like NiCo2O4 nanowires with different exposed reactive Planes for high-performance supercapacitors, J. Mater. Chem. A Mater. 1 (30) (2013) 8560, https://doi.org/10.1039/c3ta11361b.
[44] P. Wang, Z. Liu, C. Han, X. Ma, Z. Tong, B. Tan, Cu2O/CuO heterojunction formed by thermal oxidation and decorated with Pt co-catalyst as an efficient photocathode for photoelectrochemical water splitting, J. Nanopart. Res. 23 (12) (2021) 268, https://doi.org/10.1007/s11051-021-05383-2.
[45] R. Thangarasu, B. Babu, N. Senthil Kumar, M.-S. Ho, O.N. Balasundaram, T. Elangovan, Impact of cu doping on the structural, morphological and optical activity of V2O5 nanorods for photodiode fabrication and their characteristics, RSC Adv. 9 (29) (2019) 16541–16553, https://doi.org/10.1039/C8RA07717G.
[46] J. Judith Vijaya, G. Sekaran, M. Bououdina, Effect of Cu2+ doping on structural, morphological, optical and magnetic properties of MnFe2O4 particles/sheets/flakes-like nanostructures, Ceram. Int. 41 (1) (2015) 15–26, https://doi.org/10.1016/j.ceramint.2013.10.145.
[47] Q.-Q. Ren, Z.-B. Wang, K. Ke, S.-W. Zhang, B.-S. Yin, NiCo2O4 nanosheets and Nanocones as additive-free anodes for high-performance Li-ion batteries, Ceram. Int. 43 (16) (2017) 13710–13716, https://doi.org/10.1016/j.ceramint.2017.07.083.
[48] A.K. Kakarla, D. Narsimulu, J.S. Yu, Two-dimensional porous NiCo2O4 nanostructures for use as advanced high-performance anode material in lithium-ion batteries, J. Alloys Compd. 886 (2021) 161224, https://doi.org/10.1016/j.jallcom.2021.161224.
[49] Q. Ouyang, Z. Lei, Q. Li, M. Li, C. Yang, A self-supported $NiCo_2O_4/Cu_xO$ nanoforest with electronically modulated interfaces as an efficient electrocatalyst for overall water splitting, J. Mater. Chem. A Mater. 9 (25) (2021) 14466–14476, https://doi.org/10.1039/D1TA00710F.
[50] J. Li, S. Xiong, Y. Liu, Z. Ju, Y. Qian, High electrochemical performance of monodisperse $NiCo_2O_4$ mesoporous microspheres as an anode material for Li-ion batteries, ACS Appl. Mater. Interfaces 5 (3) (2013) 981–988, https://doi.org/10.1021/am3026294.
[51] O.O. Taiwo, M. Loveridge, S.D. Beattie, D.P. Finegan, R. Bhagat, D.J.L. Brett, P. R. Shearing, Investigation of cycling-induced microstructural degradation in silicon-based electrodes in lithium-ion batteries using X-ray nanotomography, Electrochim. Acta 253 (2017) 85–92, https://doi.org/10.1016/j.electacta.2017.08.161.
[52] W. Chen, L. Wei, Z. Lin, Q. Liu, Y. Chen, Y. Lin, Z. Huang, Hierarchical flower-like $NiCo_2O_4$@TiO_2 hetero-nanosheets as anodes for lithium ion batteries, RSC Adv. 7 (75) (2017) 47602–47613, https://doi.org/10.1039/C7RA09024B.
[53] F. Wang, T. Feng, X. Jin, Y. Zhou, Y. Xu, Y. Gao, H. Li, J. Lei, Atomic co/Ni active sites assisted MOF-derived rich nitrogen-doped carbon hollow nanocages for enhanced lithium storage, Chem. Eng. J. 420 (2021) 127583, https://doi.org/10.1016/j.cej.2020.127583.
[54] M. Cao, W. Wu, R. Guo, Y. Liang, G. Pan, H. Wu, X. Liu, J. Zhang, Molten salt synthesis of NiCo-NiCo2O4@C nanotubes as anode materials for Li-ion batteries, J. Colloid Interface Sci. 636 (2023) 518–527, https://doi.org/10.1016/j.jcis.2023.01.030.
[55] N. Liang, X. Sun, L. Qi, S. Zhang, L. Lin, C. Dong, X. Wang, Defect engineering via copper doping on oxygen-deficient manganese oxide for durable aqueous zinc-ion battery, Energ. Technol. 10 (10) (2022), https://doi.org/10.1002/ente.202200502.
[56] X. Yin, Y. Yin, N. Wang, J. He, Z. Xie, C. Cai, Z. Peng, X. Wang, M. Li, Y. Han, Facile fabrication of a series of cu-doped Co3O4 with controlled morphology for alkali metal-ion batteries, Colloids Surf. A Physicochem. Eng. Asp. 656 (2023) 130459, https://doi.org/10.1016/j.colsurfa.2022.130459.
[57] A. González-Banciella, D. Martinez-Diaz, M. Kundu, M. Sánchez, A. Ureña, Cu-doped MOF-derived α-Fe2O3 coatings on carbon Fiber fabric as Li-ion and Na-ion battery anodes for potential structural batteries, J. Power Sources 630 (2025) 236071, https://doi.org/10.1016/j.jpowsour.2024.236071.
[58] Z. Abbas, T.H. Bokhari, Z. Rana, S. Ijaz, E. Gul, A. Zafar, S. Javaid, M. Gul, K. Maaz, S. Karim, G. Xiang, M. Ahmad, A. Nisar, Mesoporous Mo-doped $NiCo_2O_4$ nanocrystals for enhanced electrochemical kinetics in high-performance lithium-ion batteries, RSC Adv. 15 (17) (2025) 13552–13560, https://doi.org/10.1039/D5RA00918A.
[59] J. Zhang, Y. Chen, R. Chu, H. Jiang, Y. Zeng, Y. Zhang, N.M. Huang, H. Guo, Pseudocapacitive P-doped NiCo2O4 microspheres as stable anode for lithium ion batteries, J. Alloys Compd. 787 (2019) 1051–1062, https://doi.org/10.1016/j.jallcom.2018.12.275.
[60] Y. Ren, X. Li, Y. Wang, Q. Gong, S. Gu, T. Gao, X. Sun, G. Zhou, Self-template formation of porous yolk-Shell structure Mo-doped NiCo2O4 toward enhanced Lithium storage performance as anode material, J. Mater. Sci. Technol. 102 (2022) 186–194, https://doi.org/10.1016/j.jmst.2021.05.079.
[61] T. Liu, X. Chen, H. Chen, C. Huang, P. Yu, W. Tang, Synergistic engineering of fluorine doping FexMn1-XMoO4/graphene heterojunction as ultrahigh-rate anode for LIBs, Sci. Rep. (2026), https://doi.org/10.1038/s41598-026-55355-6.